Materials Science-Poland, 39(3), 2021, pp. 436-445
http://www.materialsscience.pwr.wroc.pl/
DOI: 10.2478/msp-2021-0035

Investigation of porosity behavior in SLS polyamide-12 samples using *ex-situ* X-ray computed tomography

Grzegorz Ziółkowski[1,*], Emilia Grochowska[1], Dawid Kęszycki[1], Piotr Gruber[1], Viktoria Hoppe[1], Patrycja Szymczyk-Ziółkowska[1], Tomasz Kurzynowski[1]

[1]Centre for Advanced Manufacturing Technologies – Fraunhofer Project Center, Department of Laser Technologies, Automation and Production Management, Faculty of Mechanical Engineering, Wroclaw University of Science and Technology, Lukasiewicza 5, 50-371 Wroclaw, Poland

The paper presents a detailed description of the method of carrying out static tensile tests in *ex-situ* X-ray computed tomography (XCT) conditions. The study compares samples manufactured with the use of additive technology in two orientations, horizontally and vertically, which correspond to the in-layer and between-layer sintering mechanisms. Both the fracture mechanism and porosity behavior differed significantly for the two manufacturing directions. The conducted analysis made it possible to compare the changes in porosity, the number of pores, and also their diameters and shape before and after the tensile test. This allows for in-depth identification and better understanding of the phenomena occurring during the static tensile test of polyamide-12 samples manufactured using selective laser sintering (SLS) technology.

Keywords: *X-ray computed tomography, ex-situ, selective laser sintering, polyamide-12*

1. Introduction

The ability to characterize the internal structure of materials obtained with the use of various manufacturing techniques is one of the main advantages of X-ray computed tomography (XCT) [1]. Non-destructive testing with XCT is particularly important for additive manufacturing (AM) methods. The layered nature of the material processing procedure involved in AM, and the large number of factors influencing the process, increase the probability of defects or discontinuities occurring in elements produced by AM methods [2]. In this case, the quantitative assessment of the geometry of a material using the XCT method with a resolution of several micrometers allows for the optimization of the manufacturing process or the approval of the manufactured parts for production [3].

One of the most popular elements among the group of AM techniques, which is increasingly used to produce functional parts, is selective laser sintering (SLS). This technique uses thermoplastic materials as a feedstock, especially polyamides, which are the most commonly used kind of material in the AM market [4–6]. In practice, polyamide-12 is the most widely used of all processed polymer materials employed in AM technology, and the annual consumption balance is around 2,000 tons, with a growth rate of 15% year on year [7, 8]. In the present study, a powder polyamide-12 was used, and its main advantages are high mechanical strength and low melt viscosity and also good thermal stability and chemical resistance [9, 10]. Although the SLS process is characterized by high efficiency when compared to other AM methods, it is not without its drawbacks. The main disadvantages of the described technology include the anisotropy of their mechanical properties [11], as well as their porosity, which is related to the in-layer and between-layer sintering mechanisms [12]. There is a significant number of publications which describe the characteristics of manufactured elements with regard to the evaluation of process parameters (power, energy, temperature) and scanning strategies based on the verification of porosity [6–8] or mechanical properties of the produced test samples [13, 14]. Partic-

* E-mail: grzegorz.ziolkowski@pwr.edu.pl

© 2021. This is an open access article distributed under the Creative Commons Attribution-NonCommercial-NoDerivatives 4.0 License. (http://creativecommons.org/licenses/by-nc-nd/4.0/)

ularly interesting are the studies that allow for the combination of mechanical tests with synchronous imaging of the internal and external structure of samples, which is possible thanks to the use of XCT. Such tests are carried out under *in-situ* conditions [15], when the sample is subjected to a tensile test with simultaneous imaging of its damage behavior, or in *ex-situ* conditions [16], where the sample is imaged at least twice before and after the mechanical test. In both cases, an insight into the behavior of the internal structure of the tested objects is gained during functional research, when the tests are conducted during the interaction of a force.

Mechanical testing and microscopic observations of fractures allow for the evaluation and identification of factors influencing the cracking mechanism. The application of the XCT method supplements this information with the observation of the behavior of pores inside the stretched samples [17], and also provides additional information in the form of changes in the shape of the pores, and their connection or nucleation. Such information can be used to prepare and validate numerical simulations [16, 18] or to design the geometry for AM technology [19]. Therefore, the purpose of this article is the investigation of polyamide-12 samples manufactured with SLS technology using the *ex-situ* XCT tensile test.

2. Materials and method

2.1. SLS sample manufacturing

The system employed for the manufacturing of the test samples using SLS technology was EOS Formiga P110 (EOS GmbH, Krailling, Germany), and the feedstock material was polyamide-12 powder (PA2200) supplied by EOS. Refreshed powder was used, which is a mixture in a proportion of 50:50 (used: virgin). The manufacturing process was carried out using dedicated parameters (provided by the manufacturer) for this type of powder, with the processing temperatures being set to 166.5°C on the print surface, and 148°C in the removing chamber. The samples (five for each series) were produced (according to ISO-527 type 5b '*Plastics – Determination of tensile properties – Part 1 and 2'*) in two orientations in relation to the build direction – horizontal (XY) and vertical (ZX) (Figure 1A). Pictures of the samples after the *ex-situ* tensile test are shown in Figure 1B.

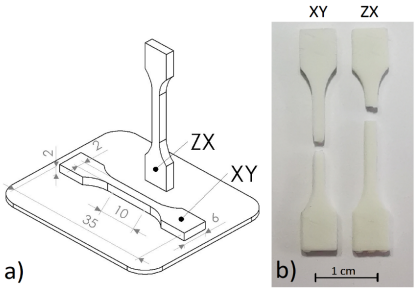

Fig. 1. Tested samples; **(A)** geometry and build orientation, XY – horizontal, ZX – vertical, **(B)** samples after the *ex-situ* tensile test for the XY and ZX planes

2.2. X-Ray computed tomography

To obtain the 3D geometry of the polyamide-12 samples, the XCT dual-tube system phoenix v|tome|x m (GE Sensing & Inspection Technologies GmbH, Wunstorf, Germany) was used. The system is equipped with a 300 kV unipolar microfocus X-ray tube, a 180 kV transmission target nanofocus X-ray, and a high-contrast digital flat panel detector (GE DXR250). During the tests, the nanofocus X-ray tube was used, in which the molybdenum-tungsten target optimized the generated X-ray spectrum at low acceleration voltages and enhanced the detectability of low density scanned materials. The scanning parameters were: a voltage of 100 kV, a current of 320 μA, a magnification of 19.9, and a voxel size of 10 μm. A standard scan was made with a 360° rotation, with the number of projections equal to 3,000, each being the average of three single projections taken with an exposure time of 100 ms. Data reconstruction was carried out using dedicated software (phoenix datos|x 2.7.2) with default reconstruction parameters. The grayscale images were analyzed in VGSTUDIO MAX 3.3 (Volume Graphics GmbH, Heidelberg, Germany). A local segmentation method was used to obtain volumetric models of the scanned samples.

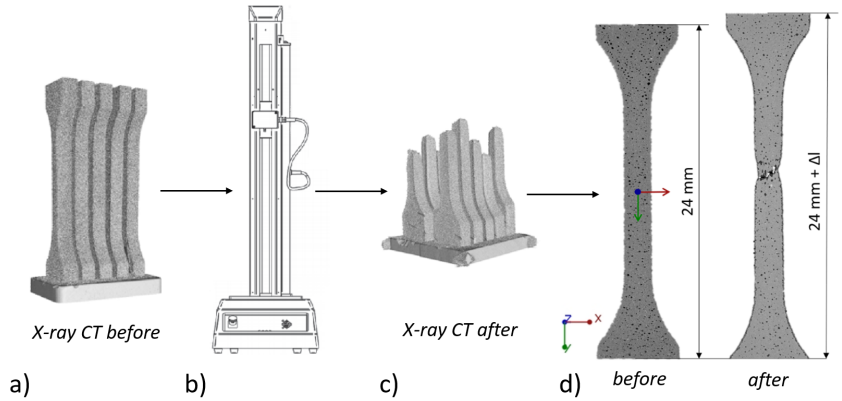

Fig. 2. *Ex-situ* tensile tests using XCT: **(A)** volumetric model of the samples before the test, **(B)** mechanical testing, **(C)** volumetric model of the samples after the tensile test, **(D)** cross-section through the sample before and after the tensile test, with the origin point marked and the main dimensions. XCT, X-ray computed tomography

2.3. *Ex-situ* XCT static tensile tests

The tensile tests were performed on the Mecmesin Multitest-I (Mecmesin Ltd, West Sussex, United Kingdom) test frame using a 1 kN load-cell (Figure 2B). The samples were mounted in wedge tensile grips, which provide better clamping with an increasing force. The tests were carried out with a 10 mm/min speed, and were continued until the samples' destruction. The test frame was connected to Emperor™ Force (Mecmesin Ltd, West Sussex, United Kingdom) software, which allowed for stress–strain characteristics to be created. The X-ray 3D reconstruction was carried out for each sample before and after the mechanical tests (Figure 2A, 2C). The samples were scanned in a stack of five at a time, but it was only the measurement area of the sample, together with a fragment of the grip part, that was subjected to XCT tests. The volumetric models of the samples obtained from the X-ray 3D reconstruction (before the tensile test) were separated and placed in the same coordinate system and at the same starting point, which is also the geometric center of the sample (Figure 2D).

The volumetric models obtained for the samples after the performed static tensile test were initially manually fitted to the geometry of the sample, which was scanned in its original state. The 'best fit' option was then used to obtain a perfect match to the initial geometry. In the next step, the top part of the sample was translated (in the given coordinate system in the y direction) by the value of absolute elongation. This approach makes it possible to compare the results before and after the tensile test in a reproducible way.

2.4. SEM investigation

Fractographic analysis using the microscopic method was carried out on fractures of the samples after the static tensile test. Analysis was performed on transverse planes of vertically and horizontally oriented samples using the Sigma VP 600 Scanning Electron Microscope (SEM) equipped with a backscattered electron (BSE) detector (Carl Zeiss, Oberkochen, Germany). For better imaging resolution and to minimize the charging effect, the samples were placed on a conductive carbon strip attached to a grounded sample holder and then covered with a thin layer of gold using a vacuum sputter coater (Quorum Q150R ES, Lewes, UK).

3. Results and discussion

3.1. Static tensile tests

The stress–strain characteristics obtained during the static tensile test are shown in Figure 3. It was not possible to determine the yield point for the produced samples, owing to the fact that the transition between the elastic and plastic behavior of

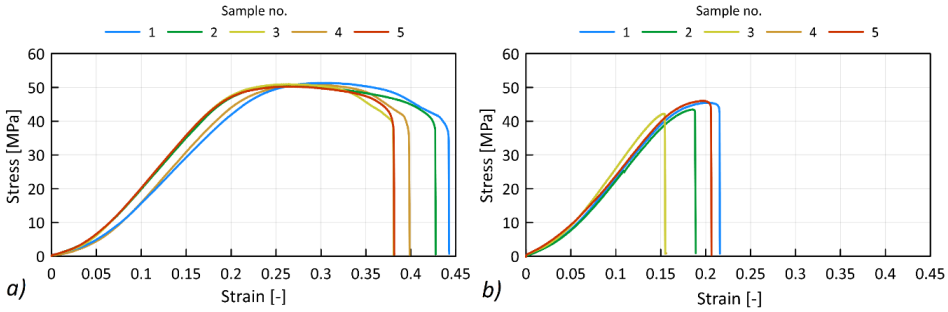

Fig. 3. Stress-strain characteristic for the: **(A)** XY plane, and **(B)** ZX plane

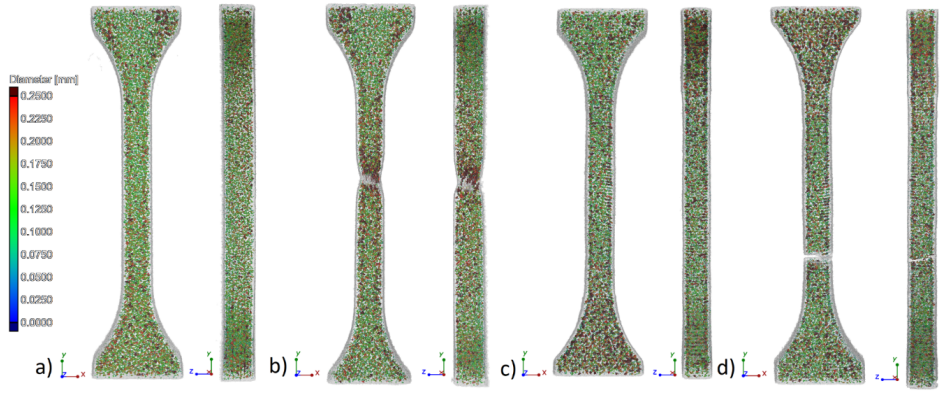

Fig. 4. XCT porosity detection; **(A)** sample XY before the tensile test, **(B)** sample XY after the tensile test, **(C)** sample ZX before the tensile test, **(D)** sample ZX after the tensile test; the force direction indicates the Y axis. XCT, X-ray computed tomography

the material was smooth. After reaching the stress value at the level of about 50 MPa (Figure 3A) for the horizontally manufactured samples, a necking could be observed, which consequently led to their complete failure. For the vertical direction, the samples behaved differently (Figure 3B) – the fracture was more brittle, and necking was not present. The lack of the neck additionally translates into the strain value, which for the ZX samples was approximately two times lower when compared to the XY samples. This contributes to lower mechanical properties than those produced in the XY direction.

The obtained results are similar to the tensile strength values presented in the literature [20, 21].

3.2. *Ex-situ* XCT

Ex-situ XCT characterization enables changes in the structure of the samples, both before and after the static tensile test, to be compared. The result of the porosity analysis, for one representative sample from each build orientation, and with the pore diameters marked in the form of colors, is shown in Figure 4. For the XY sample, porosity was 2.67% $\pm$ 0.14% and after the static tensile test it increased to 3.14% $\pm$ 0.16%, while for the ZX sample, porosity was 3.40% $\pm$ 0.08% and after the static tensile test it increased to 3.45% $\pm$ 0.09%.

Figure 5 shows, in a bubble chart, the change in porosity before and after the fracture. Each defect is shown as a circle projected onto the XY plane, and the size refers to their diameters. For the samples built in the XY direction (Figure 5A), a homogeneous dispersion without the anisotropic distribution of defects was observed. There was a visible increase in the diameter of the pores after the tensile test. For the samples built in the ZX direction (Figure 5B), the dispersion of the defect was also observed in the samples; however, the char-

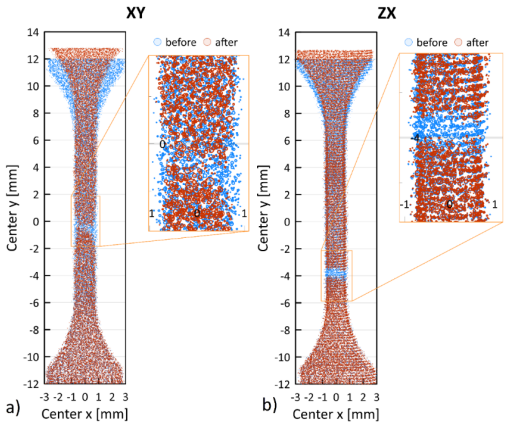

Fig. 5. Distribution of porosity along the height of the sample with regards to the pores' diameter: **(A)** XY sample, **(B)** ZX sample

acteristic growth of pores after the tensile test and their necking at the fracture area could not be observed. The anisotropy of the pore distribution related to the manufacturing direction is characteristic, i.e., the pores are arranged in layers, which indicates that the places of interlayer connections are the main cause of their occurrence.

Figure 6 shows the quantitative change of porosity corresponding to the height of the sample's gauge sections. The blue line shows changes in porosity before the static tensile test, and the red line after the fracturing of the samples. The porosity of the XY samples in the initial state ranged from 2% to 3.5%, and was homogeneous for the measured length (Figure 6C). After the static tensile test, the porosity was greater at a height of -4 mm to 6 mm of the sample, reaching a value of over 8% in the fracture area. In the case of the sample from the ZX series, the porosity for the subsequent layers ranged from 2.5 to slightly over 5% before and after the tensile test, and no significant changes in the porosity level were observed around the fracture area (red line in Figure 6F).

The number of newly registered pores after the static tensile test increased by 14% for the XY samples, and by 0.8% for the ZX samples. Most of the newly recorded pores that appeared after the tensile test were $<$50 μm in diameter (Figure 7). In the range of diameters between 60 μm and 190 μm for the samples built in the XY orientation (Figure 7A), and 60–80 μm for the samples built in the XZ orientation (Figure 7B), a smaller number of pores were observed for the samples after the static tensile tests. In this range, the pores coalesce to the greatest extent and there is a perceptible increase in their diameter.

The change in the shape of the pores can be described by a parameter that determines their sphericity, which is expressed by the following relationship (Eq. (1)):

$$\text{Sphericity} = \frac{A_{\text{Sphere}}}{A_{\text{Pore}}} \tag{1}$$

The closer the value of sphericity is to 1, the more the shape of the analyzed pore corresponds to an ideal sphere. The change in this value for all the registered pores in the tested samples is shown in Figure 8. For the XY orientations, an increase in sphericity was observed (Figure 8A). For the ZX samples, a small change in sphericity was observed, which indicates a slight change in pore geometry after the samples were stretched (Figure 8B).

The above charts refer to the entire range of the registered pores, but do not fully reveal the changes taking place for the largest pores. This is due to the significant share of newly registered pores with small diameters. Due to the limitations associated with the resolution of the XCT measurement, the shape of the smallest pores was considerably simplified, which can be inferred from their high sphericity [16]. Therefore, a further comparison was made for the pores with a minimum diameter of 20 voxels, which corresponds to a diameter of $>$200 μm. The shape comparison for the largest pores, before and after the tensile test, is shown in Figure 9. As can be seen in the figure, the shape of the pores changed the most for the samples manufactured in the horizontal direction (which can be seen from comparing Figure 9A and 9B). This is confirmed in Figure 9C, which shows the changes in the projected pore size along the force axis before and after the tensile test. In the case of the samples produced in the vertical direction, no significant changes in sphericity were observed (Figure 9D–9E). This is confirmed by the graph in Figure 9F.

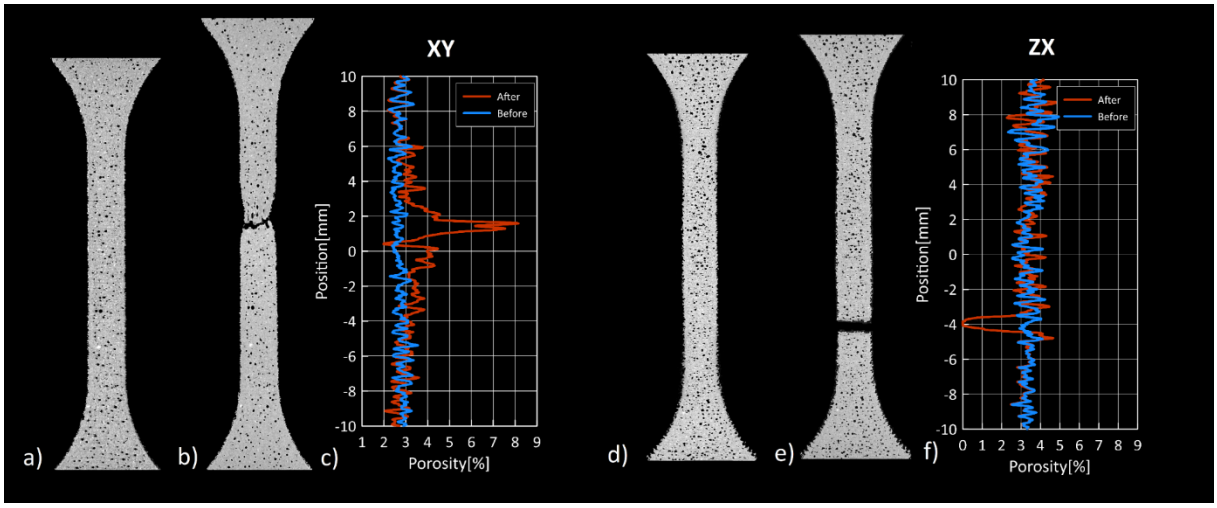

Fig. 6. Cross-section of a sample from the XY series **(A)** before, and **(B)** after the static tensile test; cross-sections of a sample from the ZX series **(D)** before, and **(E)** after the tensile test; **(C)** and **(F)** – charts that show the changes in the value of porosity in the direction that is consistent with the direction of the force

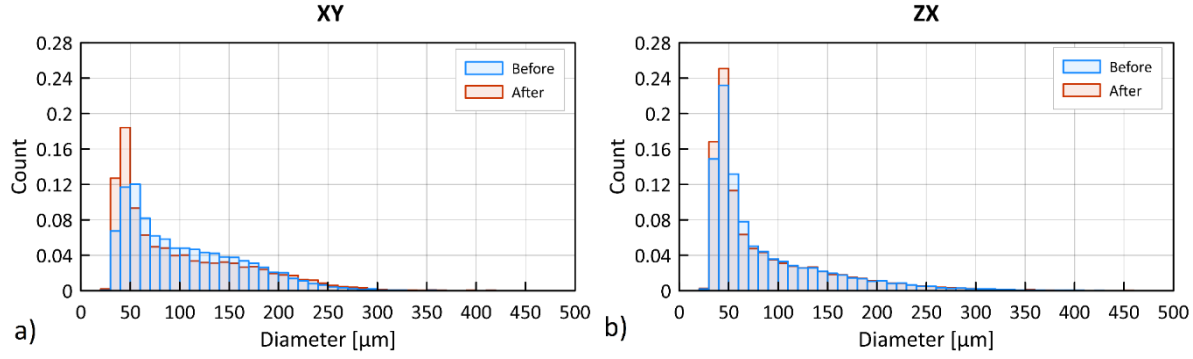

Fig. 7. Porosity recorded in an *ex-situ* test for a sample from series: **(A)** XY, and **(B)** ZX

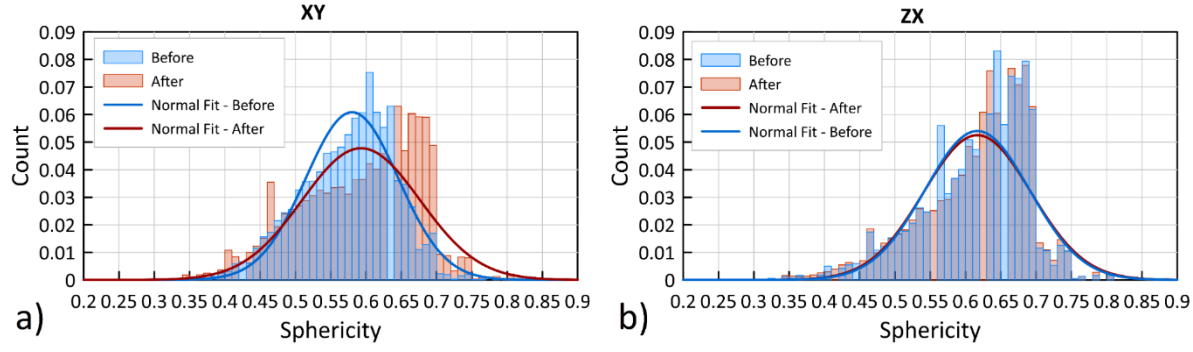

Fig. 8. Sphericity for the entire range of the registered pore diameters in an *ex-situ* test for a sample from series: **(A)** XY, and **(B)** ZX

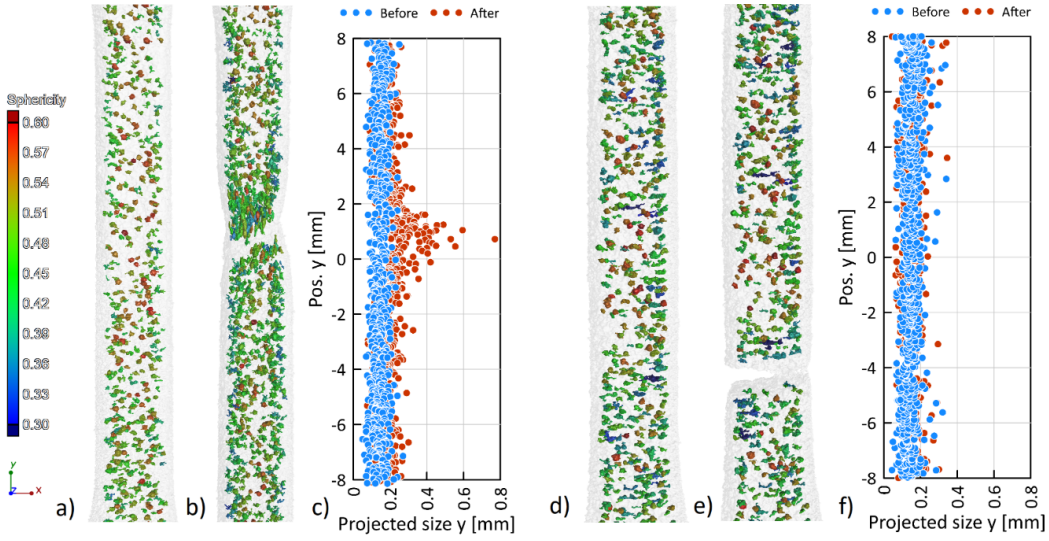

Fig. 9. Sphericity of the largest pores (diameters >200 μm), as registered in the results of the *ex-situ* test: **(A)** for sample XY before the tensile test, **(B)** for sample XY after the tensile test, **(D)** for sample ZX before the tensile test, **(E)** for sample ZX after the tensile test; (**C** and **F**) – graphs that show changes in the pore size in the XY and ZX samples along the axis of the force before and after the tensile test

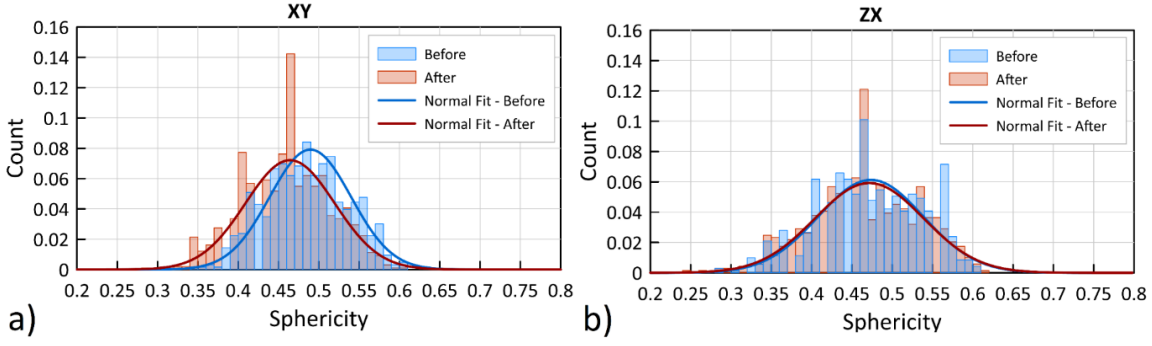

Fig. 10. Sphericity for the largest pores (diameters >200 μm) recorded in an *ex-situ* test for the sample from series: **(A)** horizontal (XY), and **(B)** vertical (ZX)

The quantitative assessment of sphericity is presented in Figure 10. A high reduction in the sphericity of the pores was observed for the XY samples (Figure 10A). A much smaller but still noticeable reduction in sphericity occurred for the ZX samples (Figure 10B).

The shapes of the pores after the tensile test for samples XY and ZX are shown in Figure 11. The presented cross-section was made in the area close to the sample's breaking point (about a millimeter above the fracture). In this case, the colors represent the surface of the porosity projected in the ZX plane of the sample's coordinate system, which corresponds to the plane perpendicular to the direction of the force.

As shown in Figure 11A, there is a reduction in the projected area of pores, which results from the formation of the neck of the sample and the elongation of the pores in the force direction. Figure 11B shows a specimen manufactured vertically; here, the pore area in the plane perpendicular to the acting force is much larger, indicating that there is a lack of pore elongation in this case.

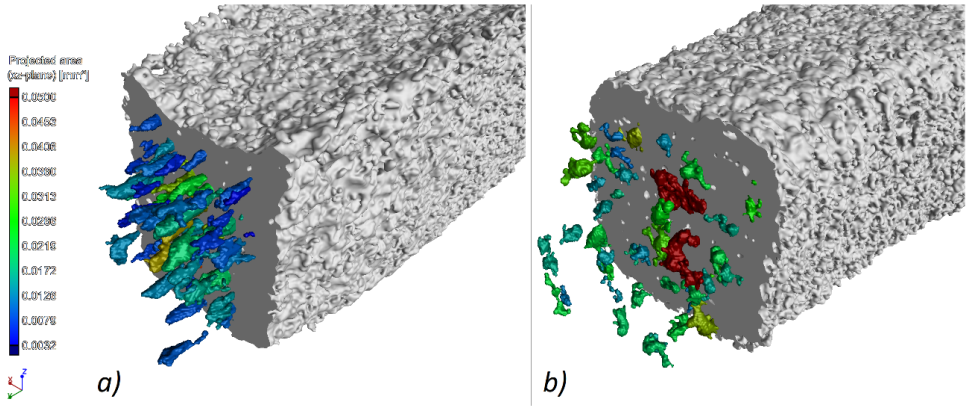

Fig. 11. Projected area in the plane perpendicular to the acting force for the largest pores (diameters >200 μm) for: **(A)** the horizontal manufacturing direction (XY), **(B)** the vertical manufacturing direction (ZX)

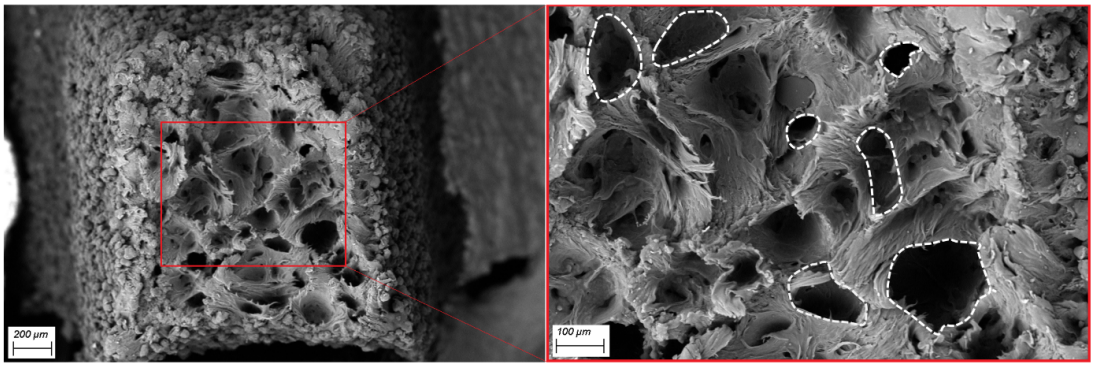

Fig. 12. Microscopic tensile post-mortem fracture images for sample manufactured in XY direction, SEM, BSE

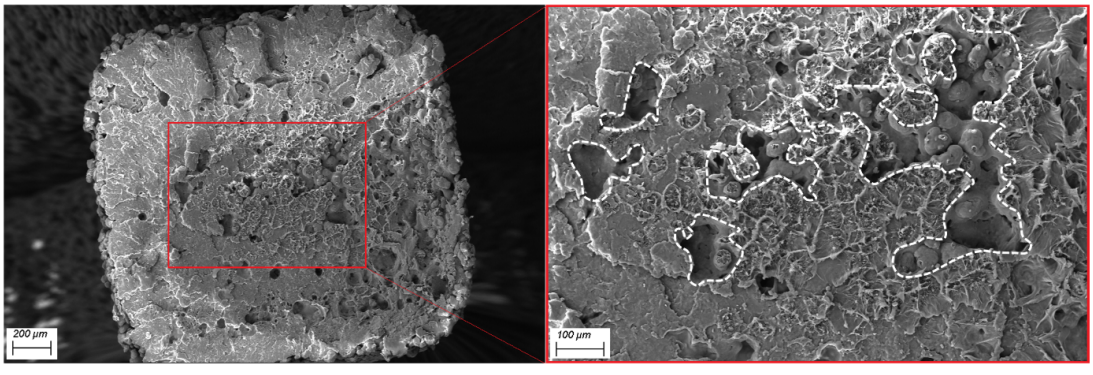

Fig. 13. Microscopic tensile post-mortem fracture images for the samples manufactured in the ZX direction, SEM, BSE

3.3. Fractography analysis

The results of the fractographic analysis complement the observations registered in the *ex-situ* XCT test. In the case of the fracture of the samples manufactured horizontally, a translaminar nature of the crack was observed (Figure 12). Pores with an oval shape and a small diameter are clearly visible here. The fibrous fracture morphology is directly related to the manufacturing direction, and

this failure mechanism is due to subsequent layers being located in the direction of the tensile force. With increasing deformation, the crack elongation occurs in the cold flow polyamide-12 matrix. The cause of the crack in this case was the coalescence and growth in the force direction of the pores.

The samples manufactured vertically demonstrate a distinct brittle fracture, which is confirmed by the obtained mechanical results. For these samples, which are characterized by layers perpendicular to the direction of the force during the tensile test, an interlaminar crack can be observed. This is due to the separation of one layer from the other (Figure 13).

In this case, pores with a large surface area and large size were noticed.

4. Conclusion

1. The volumetric porosity measured using the XCT method for the XY sample was 2.67% $\pm$ 0.14% and after the static tensile test it increased to 3.14% $\pm$ 0.16%, while for the ZX sample, the porosity was 3.40% $\pm$ 0.08% and after the static tensile test it increased to 3.45% $\pm$ 0.09%. Differences in volumetric porosity when comparing the XY and ZX build orientations can be caused by a higher ratio of contour and hatching scanning styles in the case of vertically manufactured samples.
2. After the static tensile test, a significant increase in porosity was recorded only for the samples manufactured horizontally. The number of newly registered pores after the tensile test increased by 14% for the horizontally manufactured samples, and by only 0.8% for the vertically manufactured samples. This distinction in the behavior of the samples is due to the brittle character of the vertically produced samples, which break in between the successive layers. It is caused by SLS anisotropy of the mechanical properties. The extent of variation in the observed characteristics of the vertically and horizontally manufactured samples can be attributed to the smaller surface of an individual layer when comparing these samples, as well as the variability and, as previously mentioned, scanning style ratios.
3. In order to evaluate changes in the shape of pores in the *ex-situ* XCT test, the influence of a large number of newly registered pores of a small diameter and high sphericity should be taken into account. The analysis was carried out for the pores with diameters 20 times larger than what was allowed by the resolution limit for a comparison of porosity changes with significant accuracy. The pore shape changed significantly for the samples produced horizontally, while changing only a little for the samples produced vertically.
4. Crack propagation occurred in places where no local increase in the level of porosity was observed.

Funding

This work was supported by the National Center for Research and Development in Poland (Grant No. LIDER/23/0098/L-9/17/NCBR/2018).

References

[1] Ziółkowski G, Chlebus E, Szymczyk P, Kurzac J. Application of X-ray CT method for discontinuity and porosity detection in 316L stainless steel parts produced with SLM technology. Arch Civ Mech Eng. 2014;14(4). https://doi.org/10.1016/j.acme.2014.02.003.

[2] Thompson A, Maskery I, Leach RK. X-ray computed tomography for additive manufacturing: a review. Meas Sci Technol. 2016;27(7). https://doi.org/10.1088/0957-0233/27/7/072001.

[3] Gapinski B, Janicki P, Marciniak-Podsadna L, Jakubowicz M. Application of the computed tomography to control parts made on additive manufacturing process. Procedia Eng. 2016;149(June):105–21. https://doi.org/10.1016/j.proeng.2016.06.645.

[4] Chatham CA, Long TE, Williams CB. A review of the process physics and material screening methods for polymer powder bed fusion additive manufacturing. Prog Polym Sci. 2019;93:68–95. https://doi.org/10.1016/j.progpolymsci.2019.03.003.

[5] Stansbury JW, Idacavage MJ. 3D printing with polymers: challenges among expanding options and opportunities. Dent Mater. 2016;32(1): 54–64. https://doi.org/10.1016/j.dental.2015.09.018.

[6] Yaagoubi H, Abouchadi H, Taha Janan M. Review on the modeling of the laser sintering process for Polyamide

12. E3S Web Conf. 2021;234:1–5. https://doi.org/10.1051/e3sconf/202123400006.

[7] Wohlers Associates. Wohlers Report 2020: 3D printing and additive manufacturing global state of the industry. Wohlers Associates Inc.; 2020. p. 2020.

[8] Schmid M, Wegener K. Additive manufacturing: polymers applicable for laser sintering (LS). Procedia Eng. 149(June):457–64. https://doi.org/10.1016/j.proeng.2016.06.692.

[9] Xu Z, Wang Y, Wu D, Ananth KP, Bai J. The process and performance comparison of polyamide 12 manufactured by multi jet fusion and selective laser sintering. J Manuf Process. 2019;47(July): 419–26. https://doi.org/10.1016/j.jmapro.2019.07.014.

[10] Yusheng S, Zhichong L, Haixiao S, Shuhuai H, Fandi Z. Development of a polymer alloy of polystyrene (PS) and polyamide (PA) for building functional part based on selective laser sintering (SLS). Proc Inst Mech Eng Part L J Mater Des Appl. 2004;218(4):299–306. https://doi.org/10.1177/146442070421800404.

[11] Olejarczyk M, Gruber P, Ziólkowski G. Capabilities and limitations of using Desktop 3-D printers in the laser sintering process. Appl Sci. 2020;10(18). https://doi.org/10.3390/APP10186184.

[12] Mertens JCE, Henderson K, Cordes NL, Pacheco R, Xiao X, Williams JJ, et al. Analysis of thermal history effects on mechanical anisotropy of 3D-printed polymer matrix composites via in situ X-ray tomography. J Mater Sci. 52(20):12185–206. https://doi.org/10.1007/s10853-017-1339-4.

[13] Al-Maharma AY, Patil SP, Markert B. Effects of porosity on the mechanical properties of additively manufactured components: a critical review. Mater Res Express. 2020;7(12). https://doi.org/10.1088/2053-1591/abcc5d.

[14] Zhu Z, Majewski C. Understanding pore formation and the effect on mechanical properties of High Speed Sintered polyamide-12 parts: a focus on energy input. Mater Des. 2020;194:108937. https://doi.org/10.1016/j.matdes.2020.108937.

[15] Ziółkowski G, Treter G, Tokarczyk E, Szymczyk-Ziółkowska P. New possibilities for in situ CT analysis of additive manufactured samples. Tech Trans. 2020;1–9. https://doi.org/10.37705/techtrans/e2020028.

[16] Ziółkowski G, Gruber K, Tokarczyk E, Roszak R, Ziegenhorn M. X-ray computed tomography for the *ex-situ* mechanical testing and simulation of additively manufactured IN718 samples. Addit Manuf. 2021;45(January). https://doi.org/10.1016/j.addma.2021.102070.

[17] Schob D, Sagradov I, Roszak R, Sparr H, Franke R, Ziegenhorn M, et al. Experimental determination and numerical simulation of material and damage behaviour of 3D printed polyamide 12 under cyclic loading. Eng Fract Mech. 2019;229(November):106841. https://doi.org/10.1016/j.engfracmech.2019.106841.

[18] Roszak R, Schob D, Sagradov I, Kotecki K, Sparr H, Maasch Ph, et al. Experimental determination and numerical simulation of temperature dependent material and damage behaviour of additively manufactured polyamide 12. Mech Mater. 2021;159(April): 103893. https://doi.org/10.1016/j.mechmat.2021.103893.

[19] Kok Y, Tan XP, Wang P, Nai MLS, Loh NH, Liu E, et al. Anisotropy and heterogeneity of microstructure and mechanical properties in metal additive manufacturing: a critical review. Mater Des. 2018;139:565–86. https://doi.org/10.1016/j.matdes.2017.11.021.

[20] Hou G, Zhu H, Xie D. The influence of SLS process parameters on the tensile strength of PA2200 powder. IOP Conf Ser Earth Environ Sci. 2020;571(1). https://doi.org/10.1088/1755-1315/571/1/012111.

[21] Craft G, Nussbaum J, Crane N, Harmon JP. Impact of extended sintering times on mechanical properties in PA-12 parts produced by powderbed fusion processes. Addit Manuf. 2018;22(June):800–6. https://doi.org/10.1016/j.addma.2018.06.028.

Received 2021-10-07
Accepted 2021-11-27